Lecture 9: Spatially localized structures in fluid flows

Edgar Knobloch: notes by Bevin Maultsby and Yuan Guo
with substantial editing by Edgar Knobloch

January 5, 2013

1 Defect-mediated snaking

In lecture 8 we explained the origin of the snaking-pinning region in parameter space containing a large multiplicity of spatially localized single-pulse states of ever greater length as well as a great variety of bound states of such structures called multipulse states. We also discussed the behavior of the system outside this region focusing on different types of depinning. We saw that in one spatial dimension structures in the Swift-Hohenberg equation grow by adding new cells on the outside, and examined some of the ways localized structures in two spatial dimensions grow in size as one follows them through parameter space. Certain aspects of this behavior appear to be universal in the sense that they depend only on the presence of a structurally stable transverse intersection of certain stable and unstable manifolds. However, other mechanisms for growth exist as well and we begin this lecture by describing one such mechanism that arises in the forced complex Ginzburg-Landau equation.

We consider a continuous system in one spatial dimension near a bifurcation to spatially homogeneous oscillations with natural frequency ω in the presence of spatially homogeneous forcing with frequency Ω. We focus on the behavior near strong resonances of the form $\Omega/\omega = n$, where $n = 1, 2$.

1.1 2:1 resonance

Suppose that a dynamical observable $w(x,t)$ takes the form

$$w = w_0 + Ae^{i\Omega t/n} + c.c. + \cdots$$

where w_0 represents the homogeneous equilibrium state and $A(x,t)$ is a complex amplitude. Under appropriate conditions the oscillation amplitude $A(x,t)$ obeys the forced complex Ginzburg-Landau equation (FCGL),

$$A_t = (\mu + i\nu)A - (1 + i\beta)|A|^2A + (1 + i\alpha)A_{xx} + \gamma\bar{A}^{n-1}, \tag{1}$$

as obtained in lecture 8. Here μ represents the distance from onset of the oscillatory instability, ν is the detuning from the unforced frequency, and α, β and $\gamma > 0$ represent dispersion, nonlinear frequency correction and the forcing amplitude, respectively, all suitably scaled. Figures 1(a,b) show the (ν, γ) parameter plane for $n = 2$ (subharmonic resonance) and

suitable values of the remaining parameters. The figure shows the curve $\gamma = \gamma_0$ corresponding to a subcritical bifurcation of phased-locked states from the trivial $A = 0$ state. An analysis similar to that performed for the Swift-Hohenberg equation at $r = 0$ shows that this bifurcation is also associated with a bifurcation to spatially localized states. This time these states take a top hat form (the spatial eigenvalues λ at $\gamma = \gamma_0$ are real) and there is only one branch of such states that bifurcates at $\gamma = \gamma_0$. These eigenvalues becomes complex along $\gamma = \gamma_0^T$, i.e., the bifurcation at $\gamma = \gamma_0^T$ is precisely of the type discussed in lecture 7 in the context of the Swift-Hohenberg equation.[1] The figure also shows the line $\gamma = \gamma^T$ of analogous bifurcations that occur along the upper branch of the spatially uniform phase-locked states A^+. These states are stable in time in the shaded region where the spatial eigenvalues λ are complex (region 1, lecture 6), and unstable in time outside, where the spatial eigenvalues are purely imaginary (region 4, lecture 6). The bifurcation at $\gamma = \gamma^T$ is supercritical (towards lower γ) between the two open diamonds and subcritical otherwise. The figure also shows the line of heteroclinic connections between $A = 0$ and $A = A^+$, i.e., the curve of collapsed snaking, where the localized states created at $\gamma = \gamma_0$ terminate (Fig. 2(a)). This curve, $\gamma = \gamma^{CS}$, crosses the curve $\gamma = \gamma^T$ at $\nu = \nu^*$. For $\nu > \nu^*$ the state $A = A^+$ is hyperbolic in space and heteroclinic connections involving A^+ are therefore possible. This is no longer so when $\nu < \nu^*$, where A^+ becomes a center. It follows that something new must take place as ν decreases through $\nu = \nu^*$.

Figure 2(a) shows the bifurcation diagram of solutions at $\nu = 1.35$, larger than the critical value $\nu^* \simeq 1.3077$, plotted in terms of the L^2 norm N defined as

$$N = \sqrt{\frac{1}{l}\int_{-l/2}^{l/2} |A(x)|^2 + |A_x(x)|^2 \, \mathrm{d}x},$$

while Fig. 2(b) shows the real and imaginary part of the complex amplitude $A \equiv U + iV$ at a location high up the collapsed snaking branch, labeled L_0 in Fig. 2(a). The oscillations at the fronts at either end are a reflection of the complex spatial eigenvalues of A^+ in the region $\nu > \nu^*$.

The bifurcation diagram for steady solutions at a value of $\nu = 1.26 < \nu^*$ is shown in Fig. 3. Here we can see that the behavior of the spatially homogeneous states $A = 0$ and $A^\pm$ remains similar to the previous case, but the behavior of the localized states is very different: a single snaking branch L_0 of spatially localized states bifurcates from $A = 0$ at $\gamma = \gamma_0$ but this branch must now interact with the spatially periodic solutions created at $\gamma = \gamma^T$ that surround A^+ when $\nu < \nu^*$. In standard homoclinic snaking between $A = 0$ and a periodic orbit (lecture 7) this process makes use of two intertwined branches of localized states in the form of localized wavepackets. Here, on the other hand, one starts with a single branch L_0 of top hat profiles on top of which oscillations gradually develop as one approaches the snaking region shown in Fig. 3(a). The resulting L_0 branch combines elements from the classical picture into a single branch and it does so via a distinct growth mechanism which we call defect-mediated snaking (DMS).

The growth of the localized states along the DMS branch is illustrated in Fig. 4. This branch contains two distinct families of states. One consists of uniform amplitude segments, which resemble the localized states found in regular homoclinic snaking and is represented

[1] The superscript T refers to Alan Turing since the famous Turing instability is exactly of this type.

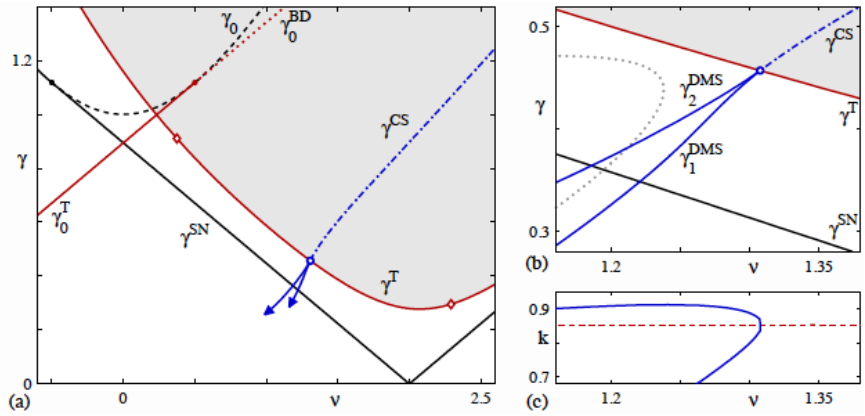

Figure 1: Parameter plane for $\alpha = -2$, $\beta = 2$ and $\mu = 1$ in Eq. (1). The curve γ_0 is plotted as a solid line in $\nu < \nu_\beta$, where the bifurcation to the uniform phase-locked states is supercritical, and dashed in $\nu > \nu_\beta$, where it is subcritical. The (solid) line γ_0^T in $\nu < \nu_\alpha$ represents a Turing bifurcation on $A = 0$. The corresponding bifurcation on the spatially homogeneous state A^+ is denoted by γ^T. The shaded region contains states A^+ that are stable in time. A heteroclinic cycle between $A = 0$ and $A = A^+$ forms along the dot-dashed line γ^{CS} corresponding to collapsed snaking. (b) Detail near the codimension-two point $\nu = \nu^*$ marked with an open circle, where collapsed snaking turns into defect-mediated snaking within $\gamma_1^{DMS} < \gamma < \gamma_1^{DMS}$. The dotted line shows the pinning region $\gamma_2^{HS} < \gamma < \gamma_2^{HS}$ containing regular homoclinic snaking. (c) The solid line shows the wavenumber range included in defect-mediated snaking as a function of ν. The dashed line shows $k_T(\nu)$. The wavenumber range shrinks to $k_T(\nu^*)$ as ν increases towards ν^*. From [10].

by solid lines. The other consists of defect segments, shown by means of dashed lines. Figure 4 shows that the DMS branch alternates between two types of uniform amplitude segments: those where $V(x)$ has a minimum at $x = 0$ (labeled by the spatial phase $\Phi = 0$) or maximum at $x = 0$ (labeled by the spatial phase $\Phi = \pi$); these two segments are separated by a defect segment. Evidently the defect is a steady state analog of a pacemaker: as one proceeds up the DNS branch the defect at $x = 0$ repeatedly splits in two thereby inserting a new wavelength into the localized states and pushing the existing cells apart.

The oscillatory wavetrain high up the DMS branch necessarily resembles the periodic wavetrain created at $\gamma = \gamma^T$ provided this wavetrain is hyperbolic in space. It turns out that this requirement corresponds to a region of the (γ, k) plane called the Eckhaus-stable region [7]. In this region a periodic wavetrain with wavenumber k is stable in time (Fig. 5, region I), while outside this region the wavetrain is unstable with respect to phase slips (Fig. 5, region II), which force the wavenumber into the Eckhaus-stable region. In region II all Floquet multipliers of the wavetrain lie on the unit circle and the wavetrain is nonhyperbolic. Consequently no heteroclinic connections involving such a wavetrain are possible. It follows that in this case the boundary of the snaking or pinning region is determined by the requirement that the wavenumber k at γ_1^{DMS} and γ_2^{DMS} is neutrally

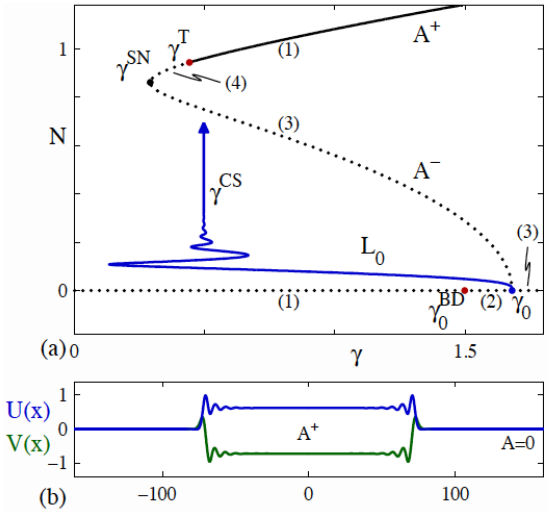

Figure 2: Bifurcation diagram corresponding to the $\nu > \nu^*$, where the branch of localized states undergoes collapsed snaking towards $\gamma = \gamma^{CS} > \gamma^T$. The localized states are everywhere unstable but are shown as a solid line. The remaining solid (dotted) lines correspond to stable (unstable) homogeneous states. (b) A sample solution far up the collapsed snaking branch, at $\gamma \approx \gamma^{CS}$. From [10].

stable with respect to the Eckhaus instability (Fig. 5, end points of the curve C). In this case it is therefore the γ-dependence of the wavenumber k selected by the fronts on either side that is ultimately responsible for the boundaries of the snaking region. Although it looks like this mechanism is quite different from that discussed in lecture 8, viewed appropriately, it is in fact the same [4].

1.2 1:1 resonance

Similar behavior to that described above takes place when $n = 1$, i.e., in the 1:1 resonance, even though the $A = 0$ state is now absent and the phase symmetry $(A) \to (Ae^{2\pi i/n})$ is trivial [10]. Instead of describing this behavior we focus on different types of depinning that arises in systems of this type.

Figure 6 shows type I depinning that is associated with the top hat profiles present for $\nu > \nu^*$: the structure either expands uniformly or shrinks uniformly, unless γ is chosen such that the uniform state becomes unstable (as in Fig. 6(c)).

More interesting is type-II depinning that occurs outside of the DMS pinning region $\nu < \nu^*$. We find that, in contrast to the depinning in the Swift-Hohenberg equation, in the FCGL the fronts move by gradually deleting cells through repeated phase slips. These phase slips eliminate/insert new wavelengths into the structure and hence control the inward/outward speed of the fronts on either side of the structure. These phase slips take place at preferred locations within the structure implying that the structure grows so to speak from within, with a constant front profile at either end. The phase slips occur because the depinned fronts move, thereby compressing/stretching the structure and forcing

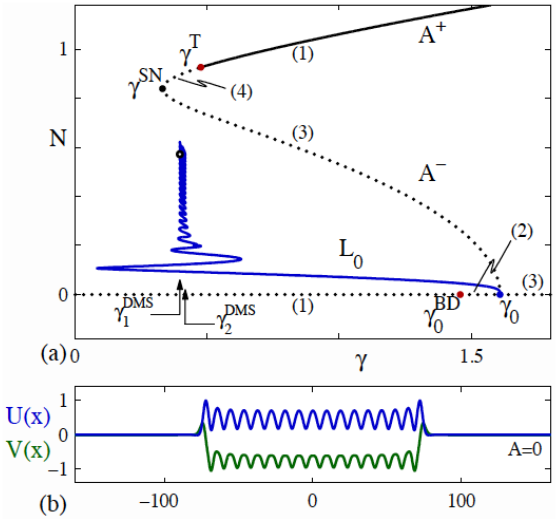

Figure 3: (a) Bifurcation diagram corresponding to the $\nu = 1.26$, where the branch of localized states undergoes defect-mediated snaking. The localized states are present within the pinning interval $\gamma_1^{DMS} \leqslant \gamma \leqslant \gamma_2^{DMS}$. The remaining solid (dotted) lines represent stable (unstable) homogeneous solutions. (b) A sample solution high up the snaking branch. From [10].

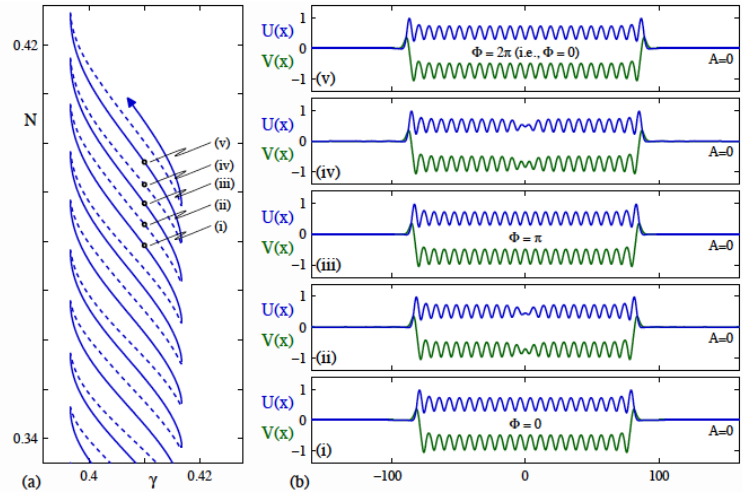

Figure 4: (a) Detail of the L_0 snaking branch. The uniform amplitude segments of the branch are shown as solid lines, while the defect segments are shown as dashed lines. (b) Five sample solutions, all at $\gamma = 0.41$. The spatial phase Φ is indicated for each profile on a uniform amplitude segment. From [10].

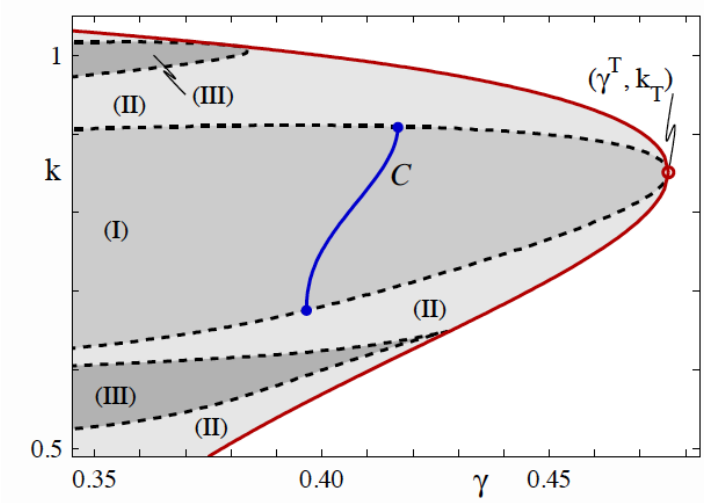

Figure 5: Section of the surface of spatially periodic states for the parameters used. The surface is bounded by the neutral stability curve of the A^+ state. The curve C shows the wavenumber $k(\gamma)$ of the patterns included in defect-mediated snaking; this wavenumber spans the width of the Eckhaus-stable interval. From [10].

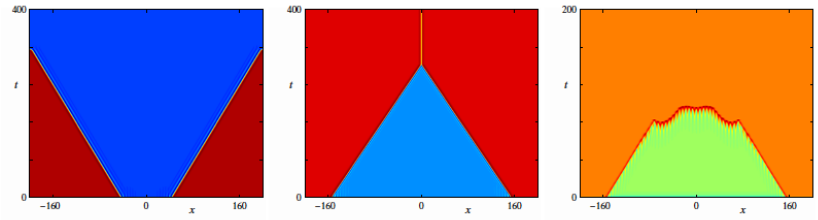

Figure 6: Type-I depinning at $\gamma = \gamma^{CS} + d_\gamma$. (a) $d_\gamma = 0.04$; (b) $d_\gamma = -0.04$; (c) $d_\gamma = -0.24$. From [10].

the wavenumber outside of the Eckhaus-stable region. The phase slip then attempts to return the wavenumber into the stable region until pattern compression/expansion moves it outside again, triggering a further phase slip.

When the structure is short the phase slips occur in the center (Fig. 7); for longer structures phase slips occur simultaneously in a pair of symmetrically located points which move inward and outward with the moving fronts (Fig. 7). We may refer to the former case as slow depinning and the latter as fast depinning. Similar phase slips eliminate phase when a nonlinear wave is incident on a solid boundary [15]. Figure 8 looks at this process in more detail.

Evidently in this type of problem the front speed is determined by the competition between natural front motion and the ability of the phase slips to keep up. This is a subtle process that remains incompletely understood [11].

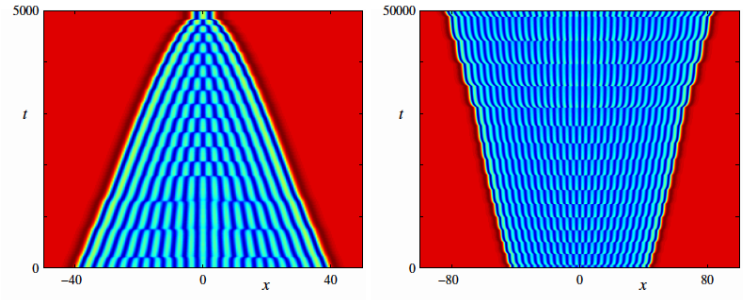

Figure 7: Type-II LS depinning at (a) $\gamma = \gamma_1^{DMS} - 1 \times 10^{-3}$; (a) $\gamma = \gamma_2^{DMS} + 1 \times 10^{-4}$. From [10].

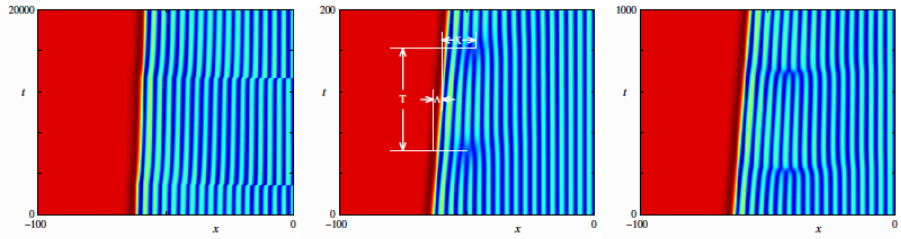

Figure 8: Type-II depinning: (a) Slow depinning ($d - \gamma = -2 \times 10^{-5}$): phase slips take place at the center $x = 0$. (b) Fast depinning ($d_\gamma = -4 \times 10^{-3}$): phase slips take place at a constant distance from the moving front. (c) Intermediate case ($d_\gamma = -1 \times 10^{-3}$): phase slips gradually move towards the front. From [10].

2 Spatially localized binary fluid convection

Convectons are localized convecting structures. Examples of convectons arising in several different systems were described in lecture 6. One of these systems is binary mixture convection. A binary mixture consists of two miscible components, one of which consists of larger molecular weight molecules than the other. Common experimentally studied examples are salt-water and ethanol-water mixtures. Both mixtures are characterized by cross-diffusion quantified by a separation ratio S. When $S > 0$ the lighter component of the mixture migrates towards the hot boundary while the heavier component migrates towards the cold boundary. This is a kinetic effect and indeed $S > 0$ is typical of gas mixtures. Liquid mixtures at appropriate concentrations may have $S < 0$.[2] When such a mixture is heated from below the heavier component migrates towards the lower hot boundary and this effect increases the local density and hence competes with thermal buoyancy. In the absence of diffusion effects a mixture with density that decreases in the vertical direction would be stable. This is no longer necessarily the case if diffusion effects are included. Since heat diffuses much faster than concentration temperature perturbations equilibrate rapidly while concentration perturbations do not. A fluid element displaced upwards therefore cools but retains its excess concentration which pushes it back down. If the "spring" provided by the concentration is strong enough to overcome viscosity (i.e., if S is sufficiently negative) this mechanism will lead to growing oscillations. This phenomenon, sometimes called overstability, is characteristic of binary mixtures placed in a thermal gradient. There is a second characteristic effect as well: steady convection is subcritical. This is because the concentration reduces thermal buoyancy near the lower boundary and hence delays the onset of steady convection. However, once steady convection is generated, for example, due to a finite amplitude instability, it mixes the concentration thereby reducing its stabilizing effect. Thus finite amplitude steady convection occurs more easily (i.e., for lower imposed temperature difference) than small amplitude convection.

The above physics is independent of the way the stabilizing concentration gradient is set up. In doubly diffusive convection concentration difference is imposed via the concentration boundary conditions at top and bottom. This is not easily done in the laboratory (although it is possible [14]). Here binary mixtures with a negative separation ratio have a great advantage since the required stabilizing concentration gradient is set up in response to the thermal gradient, i.e., the concentration gradient is set up in a closed container, and no contact with a concentration bath via permeable walls is required.

In the Boussinesq approximation binary fluid convection is described by the Boussinesq equation of state,

$$\rho = \rho_0(1 - \alpha(T - T_0) + \beta(C_1 - \bar{C}_1)), \qquad \alpha > 0, \beta > 0,$$

where C_1 is the concentration of the heavier component. The mass flux of the latter depends both on the concentration gradient via the usual Fick's law but also on the temperature

[2] This case is sometimes referred to as the anomalous Soret effect.

gradient via cross-diffusion, the *Soret effect*:[3]

$$\mathbf{j}_1 = -\rho_0 D(S_{\rm Soret}\bar{C}_1(1-\bar{C}_1)\nabla T + \nabla C_1).$$

Here D is the molecular diffusivity of the heavier component. The resulting system is described by the dimensionless equations

$$\begin{aligned}
\mathbf{u}_t + (\mathbf{u}\cdot\nabla)\mathbf{u} &= -\nabla P + PrR[(1+S)\theta - S\eta]\hat{\mathbf{z}} + Pr\nabla^2\mathbf{u} \\
\theta_t + (\mathbf{u}\cdot\nabla)\theta &= w + \nabla^2\theta \\
\eta_t + (\mathbf{u}\cdot\nabla)\eta &= \tau\nabla^2\eta + \nabla^2\theta
\end{aligned}$$

together with the incompressibility condition

$$\nabla\cdot\mathbf{u} = 0.$$

Here $\mathbf{u} = (u, w)$ is the velocity field in (x, z) coordinates (assumed to be two-dimensional), P is the pressure, and θ is the departure of the temperature from the conduction profile, in units of the imposed temperature difference $\triangle T > 0$ across the layer. The variable η is defined such that its gradient represents the dimensionless flux of the heavier component. Thus $\eta = \theta - \Sigma(x, z, t)$, where $T = 1 - z + \theta(x, z, t)$ and $C = 1 - z + \Sigma(x, z, t)$ is the concentration of the heavier component in units of the concentration difference that develops across the layer as a result of cross-diffusion. The system is specified by four dimensionless parameters: the Rayleigh number

$$R = \frac{g\alpha\triangle T l^3}{\nu\kappa}$$

providing a dimensionless measure of the imposed temperature difference $\triangle T$, the separation ratio

$$S = \bar{C}_1(1-\bar{C}_1)S_{Soret}\frac{\beta}{\alpha}$$

that measures the resulting concentration contribution to the buoyancy force due to cross-diffusion, and the Prandtl and Lewis numbers defined as

$$Pr = \frac{\nu}{\kappa}, \quad \tau = \frac{D}{\kappa}.$$

Here ν is the kinematic viscosity of the mixture, κ is the thermal diffusivity and l is the height of the layer. All lengths have been nondimensionalized using l while time has been nodimensionalized using the thermal diffusion time in the vertical, l^2/κ.

As in all problems of this type the boundary conditions are key. Experimentally realistic boundary conditions demand that the velocity vanishes at the top and bottom (no-slip boundary conditions) and that the boundaries are impermeable (the vertical flux of C_1 vanishes on the boundaries). We also assume that the thermal mass of the boundaries is large compared to that of the liquid mixture so that the boundaries remain at fixed temperature even while the fluid convecting. If this is the case (in practice this is rarely

[3]In this discussion we ignore the *Dufour effect* which is responsible for setting up a temperature gradient in response to a concentration gradient. This effect is small in liquids although it may be important in gas mixtures.

checked) we may suppose that the temperature fluctuation θ vanishes at the top and bottom. We thus have:

$$u = w = \theta = \eta_z = 0 \qquad \text{on} \quad z = 0, 1.$$

It remains to specify the boundary conditions in the horizontal. In the following we use either periodic boundary conditions (PBC) with period Γ in x, or Neumann boundary condition (NBC), or insulating closed container boundary conditions (ICCBC) at $x = \pm\Gamma/2$, where

$$\begin{aligned} &\text{NBC} \quad u = w_x = \theta_x = \eta_x = 0 \qquad \text{on} \quad x = 0, \Gamma, \\ &\text{ICCBC} \quad u = w = \theta_x = \eta_x = 0 \qquad \text{on} \quad x = 0, \Gamma. \end{aligned}$$

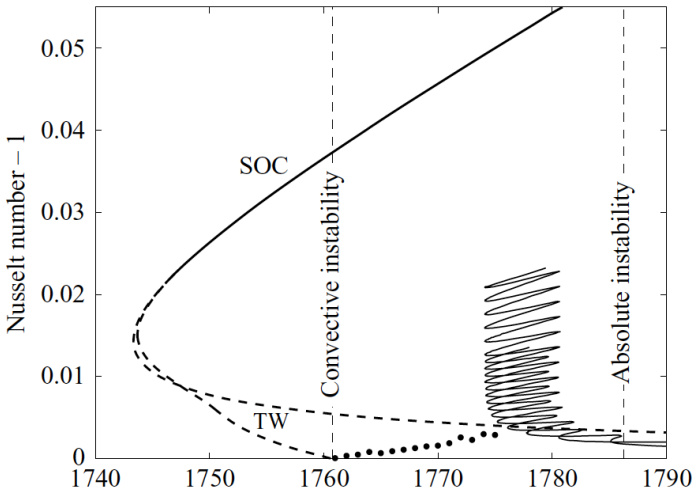

Figure 9: Bifurcation diagram showing the time-averaged Nusselt number $\overline{N}$ as a function of the Rayleigh number R when $\Gamma = 60$. The conduction state loses stability at $R_c = 1760.8$. Steady spatially periodic convection (SOC) acquires stability at a parity-breaking bifurcation marking the destruction of a branch of spatially periodic traveling waves (TW). Above threshold small-amplitude dispersive chaos is present (solid dots), which leads into the pinning region ($1774 < R < 1781$) containing a multiplicity of stable localized states of both even and odd parity. From [1].

2.1 Convectons

The above equations and boundary conditions are invariant under the symmetries $x \to -x, (u, w, \theta, \eta) \to (-u, w, \theta, \eta)$ and $(x, z) \to (-x, 1-z), (u, w, \theta, \eta) \to -(u, w, \theta, \eta)$ analogous to the symmetries $x \to -x, u \to u$ and $x \to x, u \to -u$ of SH35. We expect, therefore, the presence of steady solutions satisfying

$$\begin{aligned} &(u(x,z), w(x,z), \theta(x,z), \eta(x,z)) = (-u(-x,z), w(-x,z), \theta(-x,z), \eta(-x,z)), \\ &(u(x,z), w(x,z), \theta(x,z), \eta(x,z)) = -(u(-x,1-z), w(-x,1-z), \theta(-x,1-z), \eta(-x,1-z)) \end{aligned}$$

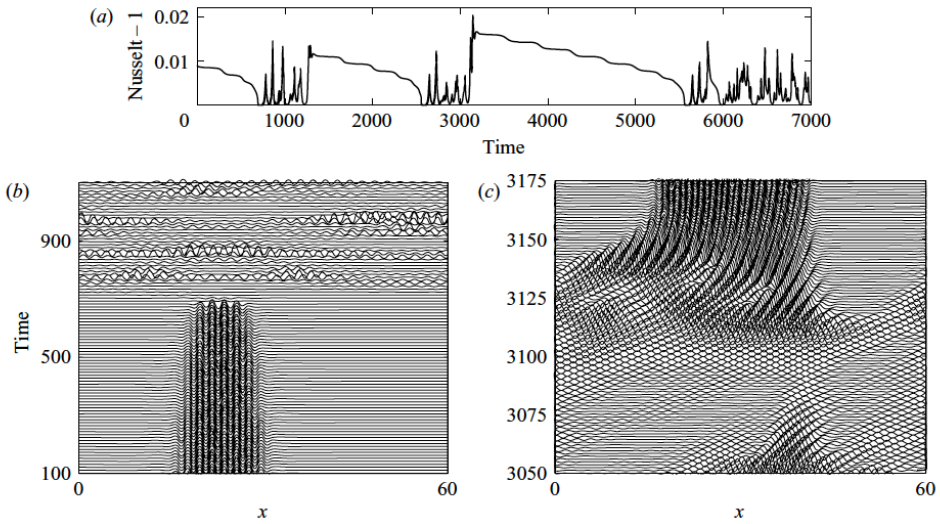

Figure 10: (a) The Nusselt number $N(t)$ at $R = 1774$ showing relaxation oscillations between dispersive chaos and localized steady convection. (b,c) Space-time plots at two different time intervals in the time series (a), showing (b) the destruction of localized steady convection, and (c) the formation of localized steady convection from dispersive chaos. Time is in units of the thermal diffusion time in the vertical. From [1].

relative to a suitable origin in x. The former have even parity and correspond to the states L_0, L_π of SH35 while the latter have odd parity when $z = 1/2$ and correspond to the states $L_{\pi/2}, L_{3\pi/2}$. These are the only steady solutions that can bifurcate from the conduction state $(u, w, \theta, \eta) = \mathbf{0}$.

Spatial stability analysis of the conduction state of the type described in lecture 7 shows that on the real line a branch of periodic states with wavenumber $k = k_c$ bifurcates from the conduction state when $R = R_c$ and that this bifurcation (if it exists and is subcritical) is accompanied by the simultaneous bifurcation of even and odd spatially localized states. As explained on physical grounds we expect the primary bifurcation to periodic states to be subcritical when S is sufficiently negative and this is indeed the case.

The equations describing binary fluid convection are not variational, however, and consequently one finds persistent time-dependent solutions as well. These are typically associated with the presence of a Hopf bifurcation from the conduction state that precedes the onset of steady convection (Fig. 9). This bifurcation generates branches of traveling and standing waves [9]. The former are subcritical (Fig. 9) implying that neither time-dependent state is stable near onset [9]. Instead one finds that the solution takes the form of a spatiotemporally chaotic states called dispersive chaos ([3], solid dots in Fig. 9). Numerical time-integration shows that this state undergoes a rapid focusing instability as R increases, forming transient localized structures (Fig. 10(b,c)) which then gradually erode in the same manner as one finds in SH35 and ultimately collapse back into spatiotemporal chaos. Since this state is unstable to the focusing instability, the process repeats, generating a chaotic relaxation oscillation (Fig. 10(a)). The successive localized states tend to form in the same location because the collapsing structure leaves a footprint in the slowly diffusing concentration field.

A very small increase in R, to $R = 1775$, suffices to stabilize the localized structure against erosion and the localized state that grows out of the chaotic state remains stable for the duration of the simulation [1]. Based on the study of SH35 described in lecture 8 we interpret this transition as passage from outside to inside of the pinning region. Of course the present system yields an eighth order dynamical system for steady states so one needs to be careful with this type of argument but here it appears as if the additional dimensions do not play a role.

It is important to observe that when the localized structure is present the waves in the background disappear, creating a localized state embedded in a quiescent background conduction state. At first sight this is surprising since, as already mentioned, the conduction state is unstable to oscillations. Batiste et al. [1] show that in the regime where waves are absent the conduction state is only convectively unstable. This means that a localized disturbance propagates faster than it grows[4] and so interacts with the localized structure before it has had a chance to develop. The collision with the localized structure reduces locally the length scales and hence enhances dissipation. In fact, in the convectively unstable regime the presence of nonperiodic boundaries always leads to eventual decay [15] and this is the case here as well. To get sustained waves in the background one must raise the Rayleigh number R past the threshold for absolute instability (Fig. 9); this threshold can be computed by solving a linear boundary value problem [1]. The solution determines the dispersion relation $\omega(k)$ as a function of R. At the absolute instability threshold $R = R^*$ this relation has a double root $\omega(k)$, provided a certain pinching condition holds. However, the double root is usually located in the complex k plane and hence the boundary value problem that has to be solved is in fact complex-valued. This requirement together with the condition of marginal stability (i.e., the requirement that ω is real) yields four conditions which suffice to determine ω, $k = k_r + ik_i$ and R^*. Figure 11 shows k_i and ω as functions of k_r at $R < R^*$ and $R > R^*$, demonstrating the presence of a double root at $R = R^*$.

Figure 9 summarizes the results in the form of a bifurcation diagram showing the (time-averaged) convective heat flux $\overline{N} - 1$ as a function of R for the parameters used. The figure shows the branch of traveling waves (TW) and indicates that steady overturning convection (SOC) remains unstable past the fold on the left and only acquires stability at a higher amplitude, where the TW branch terminates on the SOC branch in a parity-breaking bifurcation. Near this bifurcation the phase speed of the TW decreases to zero as the square root of the distance from the termination point. Stationary convectons are present in a parameter regime where the SOC are stable and it is this fact that is ultimately responsible for their stability. After all, long convectons resemble a long interval of the periodic state and so tend to inherit the stability properties of the coexisting periodic state.

To construct the unstable SOC and TW solutions (dashed lines) we have employed numerical continuation. The ability to perform such computations is key for understanding the behavior of flows of this complexity. Numerical continuation is of course particularly helpful for constructing the convecton branches. Here the fact that some of these states are stable is of great help since they can be found by direct numerical simulation. Once one even and one odd state is found in this way the equilibrated solution can be inserted into the continuation code and the whole snaking diagram constructed (Fig. 9). We mention

[4]Recall that standing waves are unstable to traveling waves.

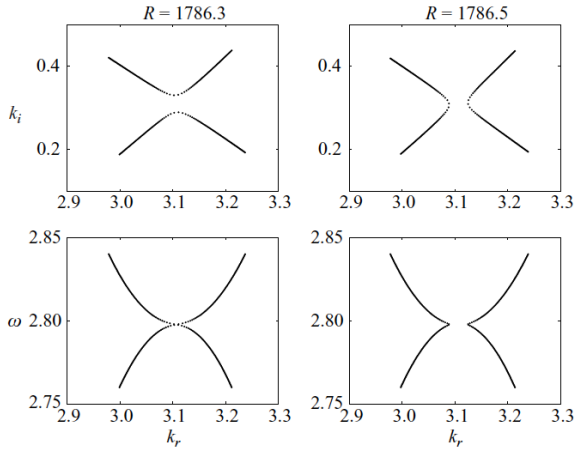

Figure 11: Spatial branches of zero growth rate modes in the complex k plane showing the pinching process that occurs at $R = R^* \approx 1786.4$, when $S = -0.021$, $\sigma = 6.22$, $\tau = 0.009$. From [1].

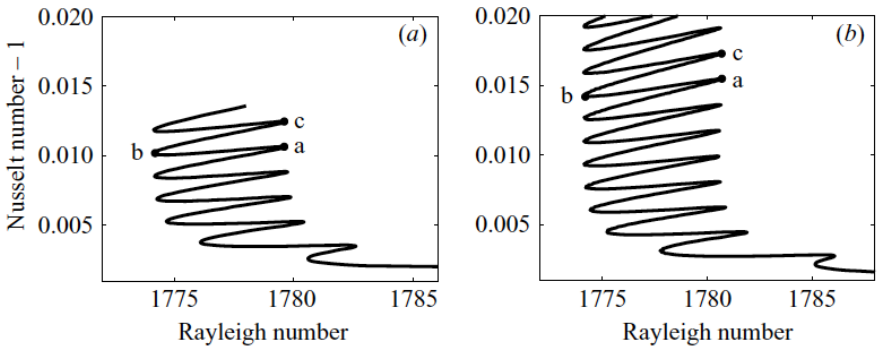

Figure 12: Branches of (a) odd- and (b) even-parity convectons in a $\Gamma = 60$ domain as a function of the Rayleigh number R. Both branches exhibit snaking. From [1].

that in the present problem the asymmetric states on the rungs of the snakes-and-ladders structure generically drift, i.e., they take the form of drifting (and unstable) convectons. Such states can be computed by looking for steady solutions in a moving frame, with the speed c of the frame determined as a nonlinear eigenvalue, much as in lecture 8. These states, like the standing waves SW created in the primary Hopf bifurcation, are not shown in the figure.

Figure 12(a) shows a detail of the snaking branch of odd parity convectons while Fig. 12(b) shows the corresponding even parity convectons. As in SH35 the solutions lying on the segments above the left folds and below the right folds correspond to stable solutions, indicating that the pinning or snaking region is populated by a large number of coexisting stable localized states (as well as periodic convection). Figure 13 shows sample convecton profiles near the folds on each branch in Fig. 12 at the points indicated. These indicate that each convecton acquires a pair of rolls between corresponding folds, one on each side,

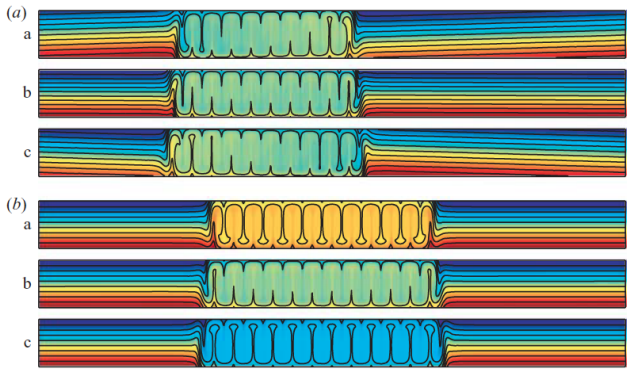

Figure 13: Convecton profiles on (a) the odd-parity branch, and (b) the even-parity branch at the turning points indicated in Fig. 12(a,b) in terms of contours of constant C. Each wavelength contains a pair of rolls. From [1].

as one goes up each snaking branch. Once again, this is exactly as in SH35. However, there is one new effect that is absent from SH35. The structure of even convectons is affected by the rolls at either end: a counter-clockwise rotating roll at the right end entrains fluid of higher concentration into the convecton, while a clockwise roll at the left does the same, thereby enhancing the mean concentration within the structure (point a in Fig. 12(b)). The opposite occurs at point c in Fig. 12(b) since the direction of rotation of outermost rolls is now opposite to that at point a. Thus at point c the structure entrains lower concentration fluid from above at both ends resulting in lower than average concentration within the structure. The effect is yet more interesting for odd parity convectons. For these states both outermost rolls rotate in the same direction, implying that at point a in Fig. 12(a) the structure entrain higher concentration fluid from the right while rejecting it on the left. This results in a pronounced concentration gradient within the structure. The net effect is that an odd parity convecton acts like a *pump*: at point a it pumps concentration from right to left, while at point c it pumps concentration from left to right. This effect is visible in the slight tilt of the constant concentration contours outside of the convecton (Fig. 13(a)).

3 Snaking in periodic and finite domains

We now look at snaking occuring in domains with different boundary conditions. To illustrate what happens when the lateral boundary conditions are changed from PBC to ICCBC we show in Fig. 14(a) the snaking diagram in a periodic domain of length $\Gamma = 14$. This is qualitatively similar to Fig. 9 except that here the whole snaking diagram has been computed. In particular we see that, when the localized structure fills almost the whole domain, snaking ceases and the snaking branches exit the pinning region and terminate on a branch of periodic states, here P_7, consisting of 7 pairs of rolls. Except for the difference in the widths of the pinning regions for even and odd states (discussed further below) the picture is as expected on the basis of SH35.

Figure 14(b) shows the corresponding result in a $\Gamma = 14$ domain with ICCBC and the same parameter values. The picture is dramatically different. The widths of the snaking

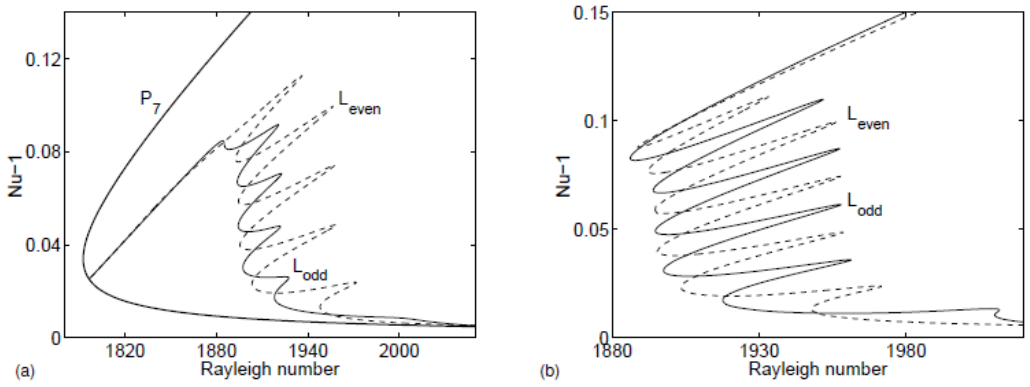

Figure 14: Binary fluid convection with $\Gamma = 14$: $S = -0.1$, $\sigma = 7$, and $\tau = 0.01$. (a) Periodic boundary conditions (PBC). (b) Insulating closed container boundary conditions (ICCBC). From [12].

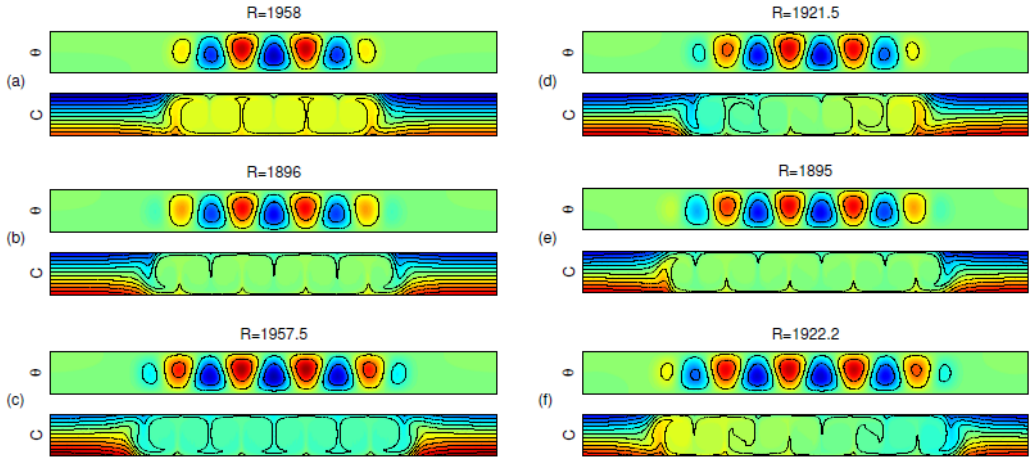

Figure 15: Convectons with PBC, $\Gamma = 14$. Profiles (a)-(c) have even parity while (d)-(f) have odd parity. From [12].

regions for the two convecton types are now identical, and the convecton branches no longer terminate on a branch of periodic states. This is, of course, because no periodic states exist with ICCBC. Instead the snaking branches continuously change into large amplitude branches of spatially extended states that fill the domain – except for defects at the lateral boundaries where the vertical velocity is required to vanish.

The fact that the ICCBC have such a large effect on odd parity convectons is a consequence of the interaction between concentration pumping and the lateral boundaries. The presence of a lateral wall in the pumping direction results in concentration build-up. As a result the convecton no longer sits in a homogeneous background, and is instead confined between two different concentrations. Such a convecton is best thought of as half of a bound state of two back-to-back odd parity convectons on a domain $\Gamma = 28$ but with PBC. This construction is in fact exact with NBC instead of ICCBC but the ICCBC results are actually quite close to the NBC results except for the vicinity of the lateral walls. Since such bound

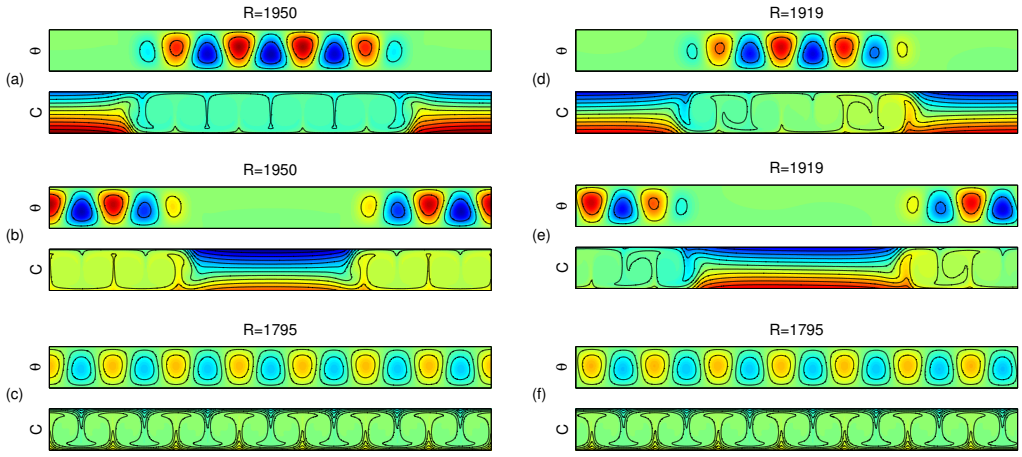

Figure 16: Convectons and holes with PBC, $\Gamma = 14$. Profiles (a)-(c) have even parity while (d)-(f) have odd parity. From [12].

states occupy the same pinning region as the one-pulse even convectons it follows that the width of odd parity states with ICCBC will be the same as the width of even parity states with ICCBC, in contrast to the PBC case.

3.1 Periodic boundary conditions (PBC)

To understand the above argument in more detail we revisit the PBC case and note that we can shift each solution horizontally by half the domain width and/or reflect it in the horizontal midplane. Consider, for example, Fig. 16. In Fig. 16(a), we see an even parity convecton inside the pinning region at $R = 1950$; to get to Fig. 16(b), we shift Fig. 16(a) by half the domain width and reflect the result in the midplane. Although there is now a hole present in the middle of the container, it is the same solution and hence falls on the same solution branch in Fig. 14. Moreover, Figs. 16(a) and (b) are phase-matched with the periodic state shown in Fig. 16(c), and in fact bifurcate from it at $R = 1795$.

We repeat this process for the odd parity states in Figs. 16(d)–(f). In this case, Figs. 16(d) and 16(e) bifurcate from the periodic state in Fig. 16(f) and do so again at $R = 1795$. This is because the periodic states in Figs. 16(c) and (f) are related by translation by half a wavelength, i.e. they are the same solutions. The even and odd parity convectons are of course different solutions. We see therefore that the bifurcation from the branch of periodic states that leads to localized states produces simultaneously two branches of such states, of even and odd parity (Fig. 14(a)). This is a generally property of Eckhaus bifurcations from a period wavetrain and can be demonstrated using Floquet theory together with weakly nonlinear theory.

However, secondary bifurcations of Eckhaus type do not always generate spatially modulated states that snake. Figure 17 shows an example of a secondary bifurcation on the branch P_6, consisting of 6 pairs of rolls within Γ, that leads to the simultaneous branching of a pair of nonsnaking branches. Close to the bifurcation these states, hereafter mixed mode states M_{even} and M_{odd}, take the form of large scale, small amplitude modulation of a

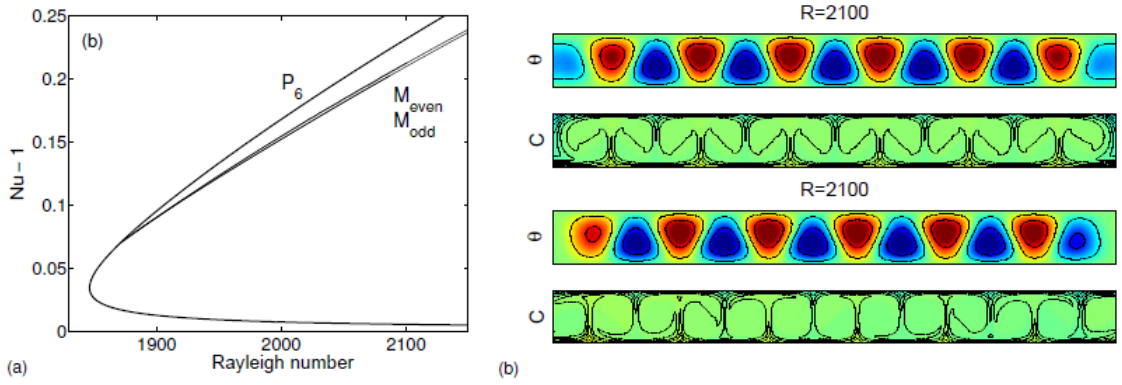

Figure 17: Mixed modes M_{even} and M_{odd} with PBC and $\Gamma = 14$. (a) Bifurcation diagram showing that both modes bifurcate from P_6 but do not snake. (b) Profiles of M_{even} (top panels) and M_{odd} (bottom panels) showing the presence of a defect at either side.

periodic wavetrain and hence resemble the hole states states discussed above. However, as one follows the hole branches away from the bifurcation point the hole deepens and broadens, and as this happens, snaking sets in. When Γ is finite the resulting states are nothing by the usual convectons, and the hole states therefore reconnect to the primary branch of periodic states when these are still of very small amplitude. In contrast, the small dip in the states M_{even} and M_{odd} does not broaden as one moves away from the bifurcation, although it deepens forming a defect in an otherwise periodic wavetrain (see Fig. 17). On the real line states of this type describe a periodic array of defects in a periodic wavetrain, with defect period Γ.

3.2 Neumann Boundary Conditions (NBC)

Neumann boundary conditions require that the lateral walls are free-slip and no-flux but translation invariance is now absent. All solutions with NBC on a domain Γ can be constructed from the set of PBC solutions with period 2Γ simply by translating the PBC solutions and keeping those that satisfy NBC on the smaller domain. This construction works because of the presence of "hidden" symmetry [5]. Observe that even solutions with NBC set in via a pitchfork bifurcation from the conduction state but set in via a transcritical bifurcation with other boundary conditions respecting reflection symmetry. Moreover, solutions with NBC have a well-defined mode number that specifies the number of "wavelengths" in the domain; in contrast, with generic boundary conditions the number of cells is not fixed, and will in general change as parameters are varied. All this is a consequence of hidden symmetry inherited from the translation invariance of the PBC problem within which the NBC problem is embedded.

In Fig. 18(a) we show an even solution at $R = 1920$ satisfying NBC with $\Gamma = 14$. The location of this solution is indicated in Fig. 18(b) using a solid dot. The solution satisfies PBC with period 2Γ, and terminates on a branch labeled SOC_{14} consisting of 14 cells within Γ. Of course SOC_{14} is the same as (a segment of) P_7 but we no longer have periodic boundary conditions and cannot therefore refer to SOC_{14} as a periodic state. Figure 18(a)

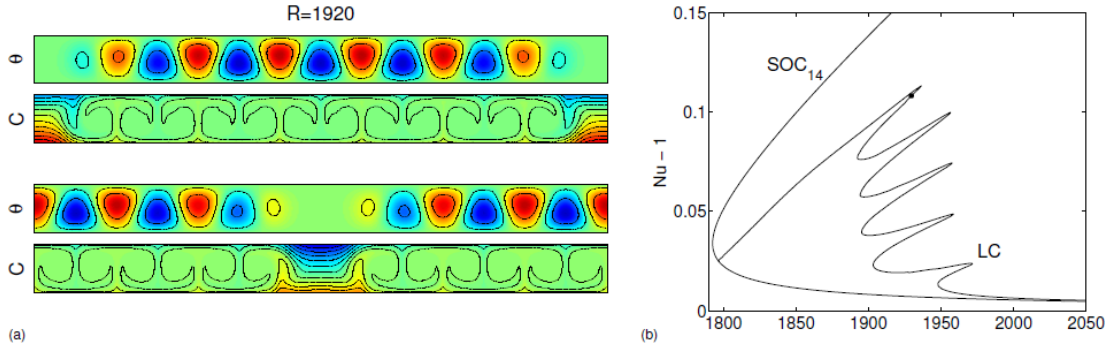

Figure 18: Even parity states with NBC and $\Gamma = 14$. (a) Convecton (top panels) and hole (bottom panel) states at $R = 1920$. These solutions are related by a hidden translation. (b) The corresponding bifurcation diagram showing a single branch of localized states LC (convectons). The dot indicates the location of *both* profiles in (a).

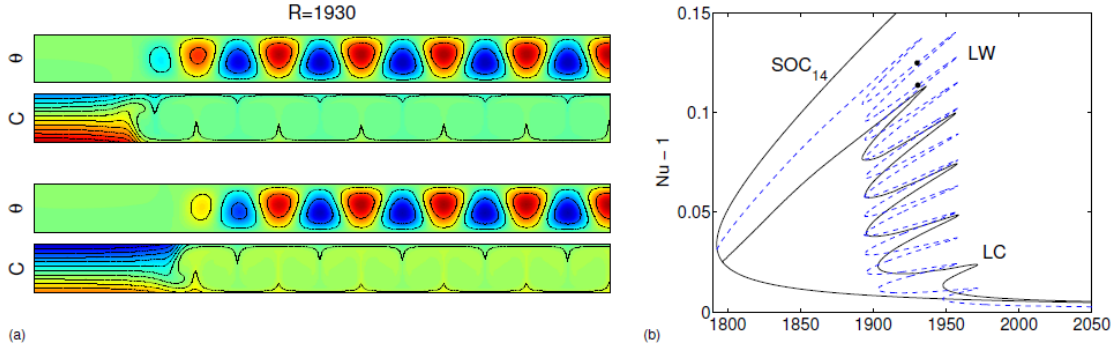

Figure 19: Wall states with NBC and $\Gamma = 14$. (a) Two different wall states LW at points indicated in the bifurcation diagram in (b). The wall states snake with double the frequency of the LC states in Fig. 18, superposed for comparison.

also shows that despite NBC (which destroy translations) we can still construct a hole state from a convecton state by embedding the problem in the PBC problem with 2Γ, performing the translations there, and reimposing NBC. It follows that there should only be one branch of localized solutions in Fig. 18(b) despite the fact that the convecton and hole states in Fig. 18(a) are not related by any of the reflection symmetries respected by NBC! All this is a consequence of the fact that with NBC one can reflect a solution in the lateral wall without introducing discontinuities ("cusps") in derivatives – a fact that guarantees that the solution with its reflection solves the partial differential equation in the doubled domain.

We can use the above procedure to construct a "wall-attached localized state," i.e., a nonlinear wall mode, as shown in Fig. 19(a). This solution also satisfies NBC with $\Gamma = 14$ and PBC with $\Gamma = 28$ and resembles the type of state computed by Ghorayeb & Mojtabi [6]. These wall modes also snake, as indicated by blue dashed lines in Fig. 19(b). The figure shows, moreover, that the snaking occurs with twice the frequency of the LC states shown in Fig. 18(a). This is because these states are really states with period 2Γ, because of the hidden symmetry, instead of the period Γ of the LC state. Because of this each back-and-

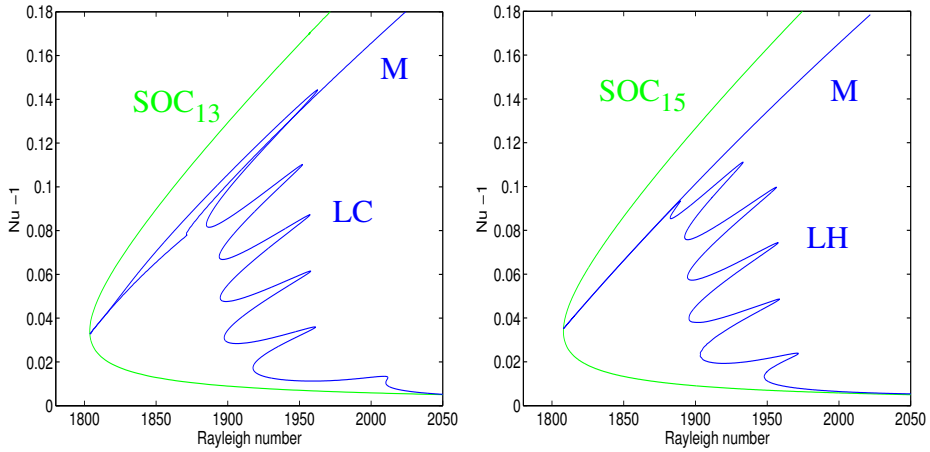

Figure 20: Odd parity states with NBC and $\Gamma = 14$. (a) Localized convectons LC terminate on SOC_{13}. (b) Localized holes LH terminate on SOC_{15}. Each termination point is accompanied by branch of even parity mixed modes labeled M.

forth oscillation on the snaking branch results in the addition of two cells to LC (one on either side) but only one cell to LW. Thus twice as many oscillations are required in order to fill the domain. Note that the larger intrinsic period 2Γ implies that the LW terminate closer to the fold on SOC_{14} than the LC branch as this distance decreases with increasing aspect ratio of the system [2].

We can also apply the above procedure to odd parity states, as shown in Fig. 20. The result is now different because convectons and holes are no longer related by a hidden symmetry. As a result the LC states terminate on the branch SOC_{13} of 13 rolls in the domain while the LH states terminate on the branch SOC_{15} of 15 rolls in the domain. Note that both SOC_{13} and SOC_{15} have odd parity. Since LC and LH now terminate on different branches it follows that each termination point must involve a second branch of modulated states as well. These missing states must have even parity since each Eckhaus bifurcation generates states of either type, and these take the form of the nonsnaking mixed modes already described (Fig. 20).

3.3 Insulating closed container boundary conditions (ICCBC)

The above construction does not work as soon as the boundary conditions differ from NBC. Nonetheless, the procedure suggests the type of states that may be present with the more realistic ICCBC. All such solutions will necessarily have defects at the boundaries owing to the no-slip velocity boundary condition. Figure 21 shows examples of even localized structures at two locations in the bifurcation diagram. As already mentioned the branch undergoes a smooth transition from snaking to a large amplitude domain-filling state with a defect at either lateral wall. This is also the case for odd parity localized structures as shown in Fig. 22. Similar bifurcation diagrams are encountered in the Swift-Hohenberg model with mixed (Robin) boundary conditions where the details of the breakup of the NBC bifurcation diagrams as the boundary conditions are changed and the transition to

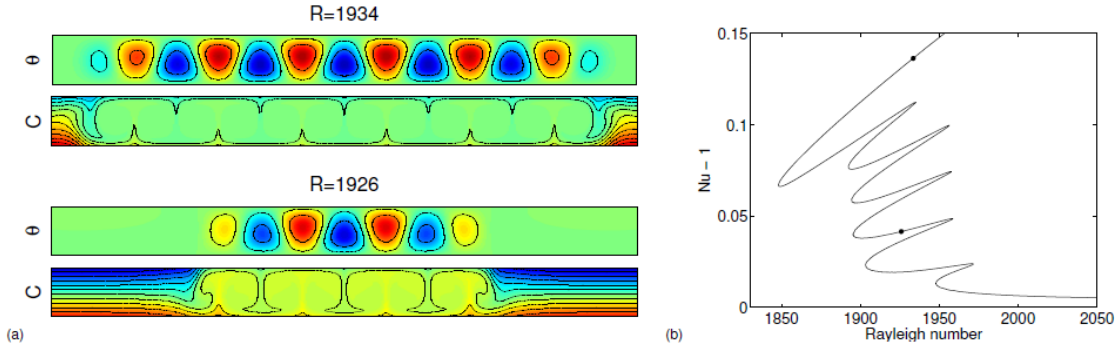

Figure 21: (a) Two different even parity convectons with ICCBC and $\Gamma = 14$. (b) The corresponding solution branch with dots denoting the location of the states in (a).

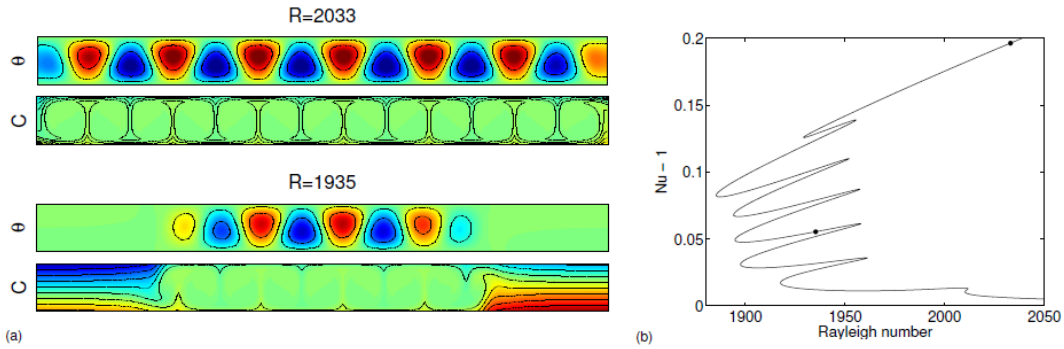

Figure 22: (a) Two different odd parity convectons with ICCBC and $\Gamma = 14$. (b) The corresponding solution branch with dots denoting the location of the states in (a).

"snaking without bistability" can be investigated [8].

Finally, we can also find examples of the wall-attached modes predicted by the NBC construction. Figure 23(a) shows two such states while Fig. 23(b) shows the corresponding solution branch (dashed), with the branch of even parity LC states superposed for comparison. We see that the LW branch oscillates back-and-forth with twice the frequency of the LC branch, exactly as in the NBC case, and for the same reason. However, once the domain is almost full the LW branch terminates on the LC branch – in the ICCBC case this is possible since the defect at the right wall can broaden sufficiently to resemble the partly filled vicinity of the left wall (or vice versa), thereby restoring reflection symmetry to the solution.

It remains to mention that the stability properties of these states have not been investigated in detail.

References

[1] O. Batiste, E. Knobloch, A. Alonso and I. Mercader, 2006. Spatially localized binary-fluid convection. *J. Fluid Mech.* **560**, pp. 149–158, 2006.

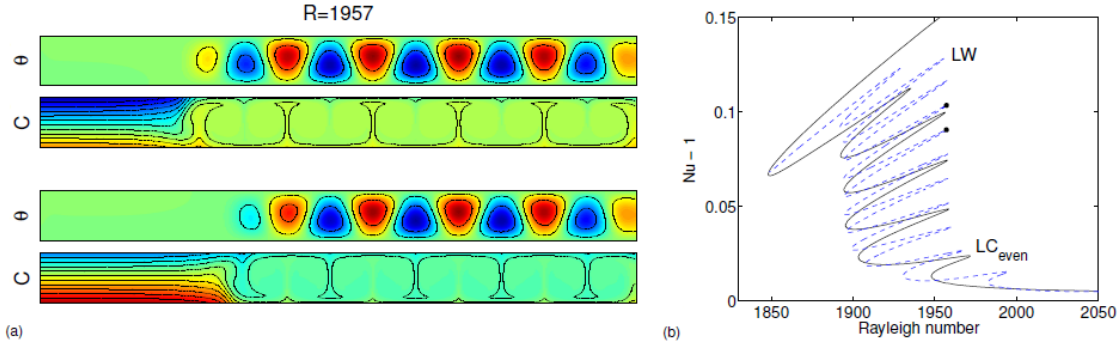

Figure 23: (a) Two wall states with ICCBC and $\Gamma = 14$. (b) The corresponding solution branch labeled LW with the LC branch from Fig. 21 superposed.

[2] A. Bergeon, J. Burke, E. Knobloch and I. Mercader. Eckhaus instability and homoclinic snaking. *Phys. Rev. E 78*, 046201, 2008.

[3] C. S. Bretherton and E. A. Spiegel. Intermittency through modulational instability. *Phys. Lett. A* **96**, pp. 152–156, 1983.

[4] A. R. Champneys, E. Knobloch, Y.-P. Ma and T. Wagenknecht. Homoclinic snakes bounded by a saddle-center periodic orbit. *SIAM J. Appl. Dyn. Syst.* **11**, pp. 1583–1613, 2012.

[5] J. D. Crawford, M. Golubitsky, M. G. M. Gomes, E. Knobloch and I. N. Stewart. Boundary conditions as symmetry constraints, in *Singularity Theory and its Applications*, Warwick 1989, Part II, M. Roberts and I. Stewart (eds), Lecture Notes in Mathematics 1463, Springer-Verlag, New York, pp. 63–79, 1991.

[6] K. Ghorayeb and A. Mojtabi. Double diffusive convection in a vertical rectangular cavity. *Phys. Fluids* **9**, pp. 2339–2348, 1997.

[7] R. B. Hoyle. *Pattern Formation: An Introduction to Methods*, Cambridge University Press, 2006.

[8] S. M. Houghton and E. Knobloch. Homoclinic snaking in bounded domains. *Phys. Rev. E* **80**, 026210, 2009.

[9] E. Knobloch. Oscillatory convection in binary mixtures. *Phys. Rev. A* **34**, pp. 1538–1549, 1986.

[10] Y.-P. Ma, J. Burke, E. Knobloch. Defect mediated snaking in the forced complex Ginzburg-Landau equation. *Physica D* **239**, pp. 1867–1883, 2010.

[11] Y.-P. Ma and E. Knobloch. Depinning, front motion, and phase slips. *Chaos* **22**, 033101, 2012.

[12] I. Mercader, O. Batiste, A. Alonso and E. Knobloch. Convectons in periodic and bounded domains. *Fluid Dyn. Res.* **42**, pp. 025505, pp. 1–10, 2010.

[13] I. Mercader, O. Batiste, A. Alonso and E. Knobloch. Convectons, anticonvectons and multiconvectons in binary fluid convection. *J. Fluid Mech.* **667**, pp 586–606, 2011.

[14] A. A. Predtechensky, W. D. McCormick, J. B. Swift, A. G. Rossberg and H. L. Swinney. Traveling wave instability in sustained double-diffusive convection. *Phys. Fluids* **6**, pp. 3923–3935, 1994.

[15] S. Tobias, M. R. E. Proctor, and E. Knobloch. Convective and absolute instabilities of fluid flows in finite geometry. *Physica D* **113**, pp. 43–72, 1998.